NanoSQUIDs based on Nb nanobridges

R. Rodrigo[1,2], M.I. Faley[1], and R.E. Dunin-Borkowski[1,3]

[1]Peter Grünberg Institute 5, Forschungszentrum Jülich GmbH, 52425 Jülich, Germany

[2]RWTH Aachen University, 52062 Aachen, Germany

[3]Ernst Ruska-Centre for Microscopy and Spectroscopy with Electrons, Forschungszentrum Jülich GmbH, 52425 Jülich, Germany

r.rodrigo@fz-juelich.de

Abstract. We have developed nanoSQUIDs with Josephson junctions in the form of Nb nanobridges, whose thickness, width and length are in the order of the superconducting coherence length in Nb thin films, which is 15 nm at 4.2 K in 20-nm-thick films. The thin Nb films were deposited using pulsed DC magnetron sputtering. A 30-nm-thick mask of PMMA resist was formed by electron beam exposure using a dose of 50 mC/cm^2 at 100 kV, at which PMMA operates as a high-resolution negative resist. Compared to the previously used HSQ resist, PMMA has a much better availability, lower health risk, a longer shelf life and a simpler development procedure, while maintaining sufficient resolution. Both Nb nanobridges with widths down to 10 nm and nanoSQUIDs with the incorporated nanobridges were fabricated using reactive ion etching with pure SF_6 gas. They show non-hysteretic *I(V)*-characteristics and a modulation of the critical current at both directly injected or externally applied magnetic field fluxes. The obtained spin sensitivity of $S_n^{1/2} \cong 135\ \mu_B/\sqrt{Hz}$ is very promising for the use of the nanoSQUIDs as magnetic field sensors for the investigation of nanoscale objects.

1. Introduction

We develop a novel low-T_c direct current nanoscale superconducting quantum interference device (nanoSQUID), that will be used for the construction of a highly sensitive scanning nanoSQUID microscope (SSM). The potential prospective applications of the nanoSQUID-microscope are measurements of nanoscale magnetic systems with single atomic spin sensitivity, nanoelectronics including memory devices, transition edge sensors for single photon and macromolecule detection, devices for quantum computing, quantum metrology, etc. [1]. Compared to magnetometers based on nitrogen-vacancies in diamond, that are currently used for nanoscale magnetic microscopy, nanoSQUIDs do not need to be illuminated by a laser, which could unintendedly heat delicate samples operating at low temperatures. Magnetic force microscopy uses hard magnetized tips that can change the magnetic state of the object while nanoSQUIDs do not contain any ferromagnetic parts. In 1983, Zimmerman and Mercerea developed the first SQUID microscope, which could perform one dimensional scans of samples [2]. The first two-dimensional scanning SQUID system for imaging was introduced by Vu and van Harlingen in 1993 [3], who introduced the term scanning SQUID microscope for the first time. Still in recent years there have been attempts to improve both the spatial resolution as well as the sensitivity of SSMs using low-T_c SQUIDs as well as high-T_c SQUIDs [4]. Troeman has developed nanoSQUIDs with incorporated 50 nm Nb nanobridges [5], but for their SSM the conventional 5 µm Nb-AlO_x-Nb Josephson junctions and an 8 µm pickup loop were used. Finkler et al.

introduced the first SSM based on a DC SQUID without a pickup coil and reached a projected spin sensitivity of 65 $\mu_B/Hz^{1/2}$ [6]. The SQUIDs are fabricated through self-alignment of the superconductor on a quartz tip and have diameters down to 100 nm. We aim to manufacture nanoSQUIDs of similar lateral dimensions on a chip using nanofabrication processes to make the sensors more robust and more customizable in the layout, while maintaining a comparable spatial and spin resolution as in ref. [6].

The Josephson junctions of our nanoSQUIDs are made in the form of Nb Dayem bridges [7] and Grooved Dayem Bridges (GDBs) [8], whose thickness, width and length are in the order of the superconducting coherence length in Nb thin films of 10 nm to 20 nm to provide the best Josephson properties for such kind of junctions [9]. Nb films are considered a dirty superconductor, which means that the electron mean free path l is limited by the concentration of impurities in the sputtered and patterned Nb films and it can be much smaller than the coherence length of ξ_0 = 40 nm of the pure bulk Nb at T = 0 K, $l \ll \xi_0$. In this case, the effective coherence length at $T > 0$ is given by

$$\xi(T) = 0.85(\xi_0 l)^{1/2}\left(\frac{T_C}{T_C - T}\right)^{1/2}$$

At T = 4.2 K, the coherence length is $\xi \cong 13$ nm for a measured superconducting transition temperature of T_c = 8 K of our $d = 12$ nm thick Nb films and an electron mean free path of $l \cong 3$ nm. The electron mean free path was calculated using the estimation for niobium thin films in the dirty limit given in ref. [10], which is $l \cong \frac{100\ \text{Å}}{1+400\ \text{Å}/d}$ and depends strongly on the preparation and storage conditions of the Nb films and nanobridges.

In our design of the nanoSQUID, the current required to bias and modulate the magnetic flux is applied directly to the SQUID loop, without the need to use additional coils for flux bias and modulation. This feature, together with the construction of the SQUID chip, will allow the nanoSQUID to be incorporated effectively into the SQUID microscope.

2. Experimental details

2.1 Thin film deposition

Mainly 350 µm thick Si substrates covered by a 300 nm thick buffer layer of SiO_2 were used. For the sake of comparison, sometimes also 1 mm thick MgO substrates were used. The substrates are first cleaned in an ultrasonic bath in acetone for 5 min. Then they are rinsed in propanol with ultrasonic agitation for another 2 min. After this, the substrates are rinsed with double distillated deionized (DI) water and dried by blow of N_2, before being placed in the sputter chamber. After reaching a sufficiently good base vacuum of under 10^{-6} mbar, 10 nm to 60 nm thick films of Nb are sputtered on the substrates by pulsed DC magnetron sputtering with Ar gas. Different superconducting transition temperatures T_c between 4.9 K and 7.7 K of 22 nm thick Nb films were measured for different sputter temperatures using a Quantum Design PPMS system (cf. Fig. 1 (a)). It can be seen that films sputtered at 100°C with no previous overnight heating show the highest transition temperature, while films that were prepared on substrates baked for several hours before sputtering show a lower T_c. Fig. 1 (b) shows an *R(T)*-measurement of a SQUID and the Nb film on the same chip. It can be seen that the transition temperature close to the SQUID is $T_c^{SQUID} \cong 7.35$ K and the SQUID resistance is $R_N \cong 17.5\ \Omega$, while for the same film further away from the SQUID one gets $T_c^{film} \cong 7.50$ K. A 1 nm thick layer of Ti is sputtered after Nb deposition on top of the Nb to promote the adhesion of HSQ resist for electron beam lithography (EBL) [12].

2.2. Electron beam exposure and development of resists

After the deposition of the Nb film, the samples are coated with electron beam resist as soon as possible to prevent the Nb from oxidation. When using HSQ (hydrogen silsesquioxane), a 2 % solution of resist is spin coated on top of the Ti adhesion layer at 4 krpm, which leads to a ca. 40 nm thick film of resist. The sample is baked for 2 min at 80 °C. As HSQ is sensitive to the time between coating and exposure, the electron beam lithography is performed as soon as possible after coating. An acceleration voltage of

50 kV, a current of 10 nA and a dose of 800 µC/cm^2 for the small structures and 1200 µC/cm^2 for the large structures, such as contacts and supply lines, are used. This way, all structures needed for the devices themselves and contacts are written in one lithography step into the HSQ resist. After exposure, a post exposure bake is performed for 2 min at 120 °C. Then the resist is developed in 25 % TMAH for 1 min, before the sample is rinsed in flowing DI water for 1.5 min.

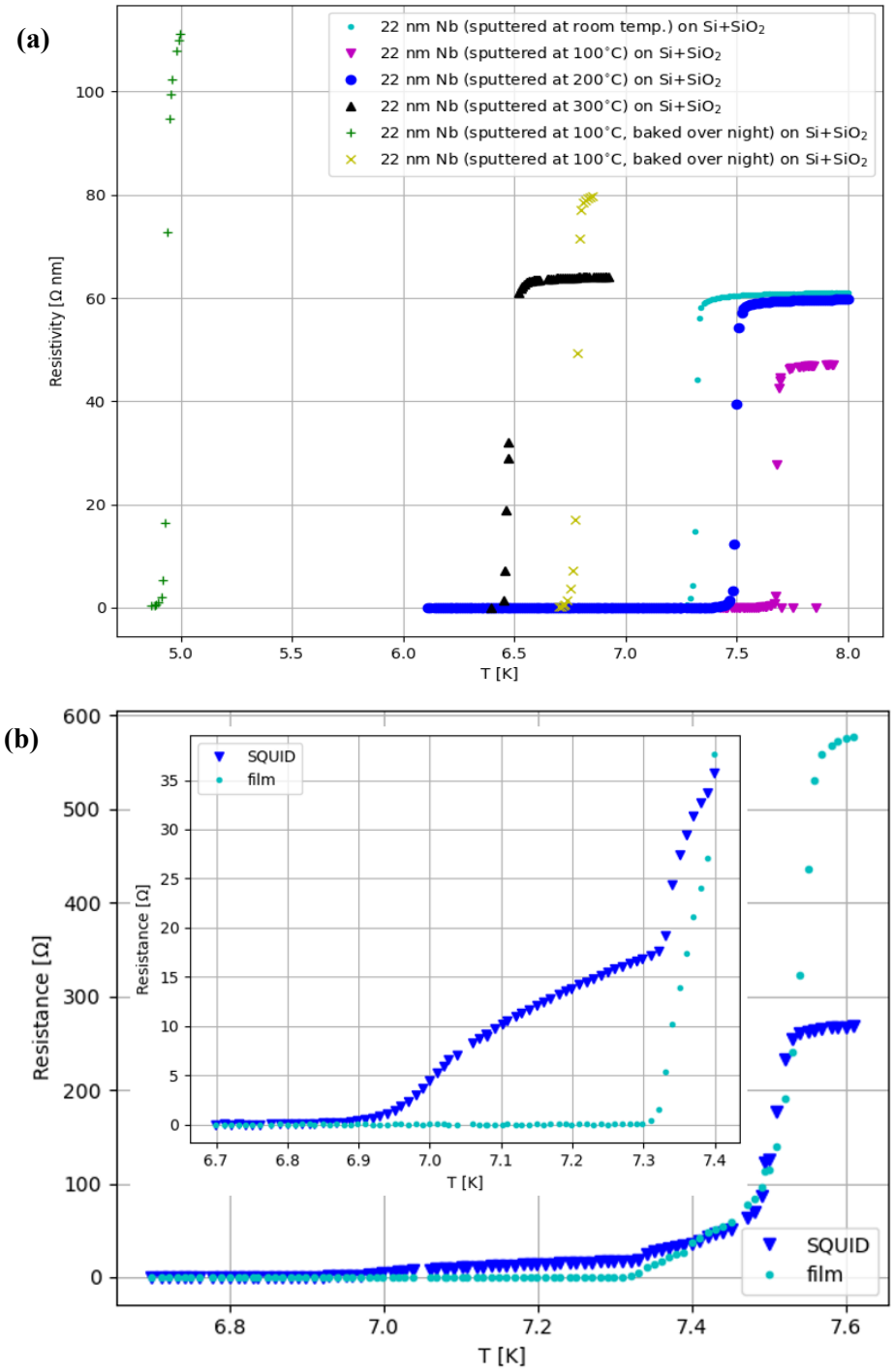

Figure 1. (a) *R(T)*-dependence of 22 nm Nb films sputtered at different temperatures and (b) *R(T)*-dependence of a SQUID and the Nb film on the same chip.

For the use of PMMA (polymethyl methacrylate, 679.02 950 K) as negative resist, it is spin coated directly after the deposition of Nb at 4 krpm and then baked for 4 min at 120 °C. After this, EBL is performed using a dose of 25 mC/cm^2 in order to use the PMMA as a high-resolution negative resist at the e-beam acceleration voltage of 50 keV and a current of 10 nA [12]. Using an acceleration voltage of 100 kV requires doubling the dose at the same e-beam current. This way, the carbon chains in the PMMA decompose into short low-molecular weight fragments that are linked to a dense carbonized film (negPMMA). This film is insoluble in acetone [13]. Due to the high dose, EBL is performed only for the small structures and not for contacts and supply lines. This procedure leads to high quality resist masks when performed on 679.02 950K PMMA resist, which has a thickness of ca. 30 nm after coating at 4 krpm. This method does not seem to work for thicker types of PMMA resist such as 670.04 950 K and so on. When exposed to the high dose electron beam, the thicker resist is perforated by holes. As pre exposure baking at 150 °C for 10 min did not change this condition, we suspect that this effect is due to escaping gases produced in the carbonization process. Lower currents seem to solve the problem but the writing time at 10 nA already exceeds an hour for our structures. After electron beam exposure, the sample is developed by moving it first in acetone, then propanol and then DI water for 1.5 min, respectively.

2.3. Photolithography

If negPMMA was used as an electron beam resist, an additional photolithography step is necessary to structure the contacts and supply lines of the sample. After the drying of the sample, it is first baked at 130 °C for 1.5 min and the photoresist UV6.06 is spin-coated at 4 krpm, which leads to a film thickness of 0.6 µm. Before exposure, the sample is prebaked at 130 °C for 1 min. Then the sample is mounted for lithography and exposed using the contact mode for 1 min. Post exposure baking is done at 140 °C for 1.5 min. The UV6 resist is developed for 1.5 min in AZ326 developer before being rinsed under DI water. Now the sample using PMMA contains a small mask of negPMMA for the devices and a broader mask of UV6 for contacts and supply lines.

2.4. Reactive Ion Etching (RIE)

After all resists are developed, RIE using pure SF_6 gas is performed on the samples, using the electron beam and photo resists as masks for structuring the underlying Nb. SF_6 has the highest selectivity towards Nb compared to both types of resist, negPMMA and HSQ. Alternative etching gases like CF_4 and O_2 show a much lower selectivity. This selectivity allows us to use thin layers of resist of only a few tens of nanometres, which enhances the resolution of the underlying etched structures.

Due to observed non-developed residuals of the UV6 photoresist around the underlying negPMMA resist, RIE using SF_6 takes longer for samples using negPMMA resist compared to HSQ. For these samples, etching times between 90 s and 100 s have proven to be ideal, depending on the specific layout and desired junction length. For samples structured using HSQ resist, etching times between 35 s and 45 s at similar other RIE parameters lead to the desired results.

As RIE is isotropic, we see an undercut of the Nb in Fig. 2 (a) due to the high selectivity of the SF_6 gas towards Nb compared to the resist. One attempt to minimize the undercut is an additional physical sputter etch step using Ar before the reactive ion etching, which is currently under testing.

2.5. Passivation

After RIE, all samples are coated with a 130 nm layer of Si using pulsed DC magnetron sputtering with Ar gas as before. This prevents the Nb film from oxidizing and acts as thermal shunt of the JJs [15]. A low resolution transmission electron microscopy (TEM) image of a test structure of Nb lines structured using HSQ covered by a layer of Si can be found in Fig. 2 (a). Using high resolution TEM, we have observed that films of Nb sputtered on textured (001) MgO substrates [11] grow epitaxially at room temperature (cf. Fig. 2 (b)). As mentioned above, the undercut created during RIE influences the growth of the Si cover layer. It therefore potentially limits the heat dissipation from the junction and has to be

minimized. Thus, so called Grooved Dayem bridges (GDBs) [7], as described in a later section, show the best results in electronic testing. In GDBs, there is no electron beam resist directly on top of the junctions, which leads to a thinner Nb film at this point, no undercut and therefore a better Si growth.

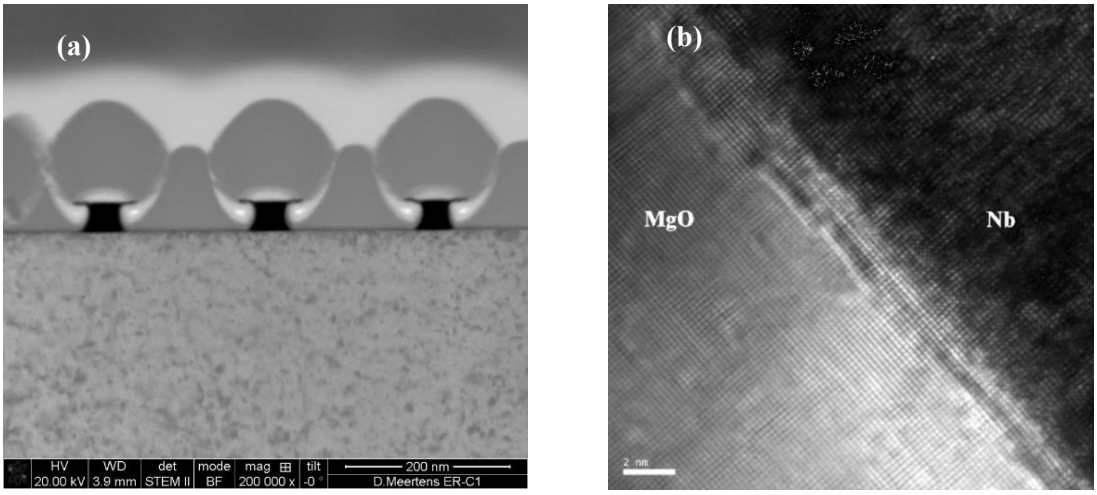

Figure 2. (a) Low resolution TEM image of Nb lines, structured using HSQ after SF_6 etching, covered by a passivation layer of Si and (b) high resolution TEM image of an epitaxial Nb film deposited on the same chip at room temperature on textured MgO substrate.

2.6. Contacts

For the HSQ samples, contacts for further electrical characterization are applied directly after RIE. A 20 nm thick layer of Pt is sputtered through a mask directly on top of the scratched part of the HSQ layer for the contact pads for a better adhesion and a galvanic contact. After that, 200 nm of Ag are sputtered on top of the Pt layer, followed by manually pressed pieces of indium. This prevents the Si from growing on the contacts during passivation of the sample.

In the case of the samples featuring negPMMA and UV6 resist, a lift-off of the UV6 is performed after sputtering Si, exposing the Nb contacts. In order to do this, the sample is placed in acetone in an ultrasonic bath for 1.5 min and then rinsed with propanol and water. After that, a Pt adhesion layer of 20 nm is sputtered onto the Nb through a mask followed by a 200 nm Ag film, which is sputtered through the same mask. At the end, pieces of indium are placed manually on the contact pads. A galvanic connection to control electronics is provided by Ag wires that are pressed to the contact pads by other pieces of indium.

3. Results and discussion

3.1 Josephson junctions

In order to fabricate a Josephson junction (JJ), it is essential to form a constriction that constrains the current flow between two superconducting electrodes. This can be done by a variety of different structure types with different tunnel barriers [8]. While tunnel junctions have been known for the longest time, we concentrate on Dayem bridges and Grooved Dayem bridges [6], as these offer a good scalability due to their two dimensional nature and a good reproducibility and temporal stability. A narrowing of the superconducting material between the two bulky electrodes reduces the critical current over the junction. Therefore, a new wave function emerges for the superconductor due to the interferences of the two wave functions of the electrodes. Compared to a classical tunnel junction with an insulating layer between two superconducting layers, Dayem bridges have some advantages. As they are created in one plane and they offer a good scalability for nanoscale applications. Furthermore, those nanobridges are

insensitive to magnetic fields applied in the plane of a SQUID device featuring two of such nanobridges, which is essential to measure e.g. nanoparticle magnetization [16].

The first layout to be transferred to the chip via lithography and RIE features seven Dayem nanobridges with lengths between 10 nm and 100 nm with contacts for electrical characterization measurements. Samples fabricated with this layout were mainly used to adjust process parameters and to test the *I(V)*-characteristics for hysteresis. Additionally, junctions structured using HSQ and PMMA were compared. All optimized parameters are given in the section above.

The bridges produced and compared using different types of resist have a length of 30 nm in the mask layout. The sample using HSQ as a resist was etched for 40 s using SF_6, while the etching time for the PMMA sample was adjusted to 90 s. This is since the second lithography step leads to longer etching times being required, as described above. This etching time is directly correlated to the exposure and development time in the photo lithography step, which were adjusted to 60 s and 90 s, respectively.

Fig. 3 shows a nanobridge junction structured using negPMMA with a length of only 10 nm in the mask in two different magnifications. As can be seen, the fabrication of nanobridges using PMMA as a negative resist with a junction length down to 10 nm is possible using the process described above.

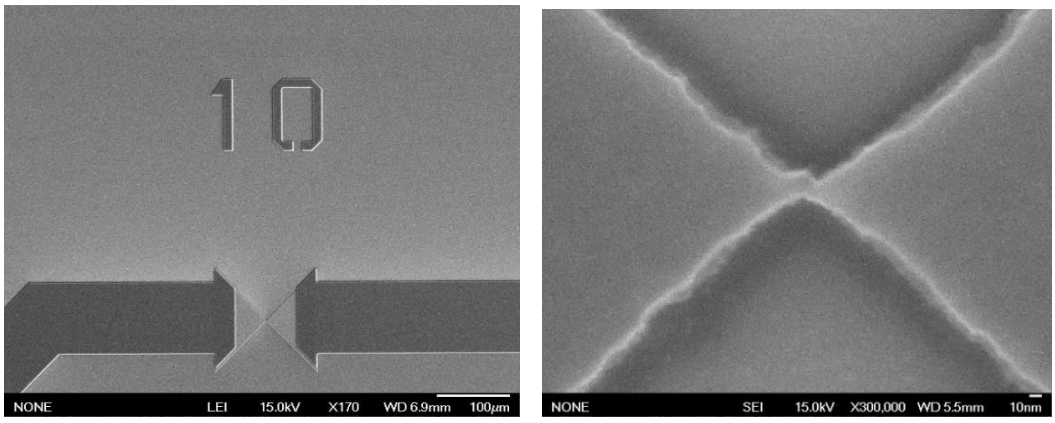

Figure 3. SEM images of a Dayem nanobridge fabricated using negPMMA with a width of only 10 nm at different magnifications.

3.2. SQUIDs featuring Dayem nanobridges and GDBs

The best-known application of Josephson Junctions is the *Superconducting quantum interference device* (SQUID), which is described in [8] in detail. It uses two JJs interrupting a superconducting loop to detect magnetic fluxes trough inductive coupling of the SQUID to the local magnetic field. By reducing the SQUID size to a few 100 nanometres, the coupling to small samples is improved, which is the prerequisite for a Scanning SQUID Microscope [16].

Using the same parameters in lithography and etching as described above, different masks can be used to structure the thin Nb film. The chip design features three supply lines per SQUID to apply voltage, current and modulation (see Fig. 4 (a)). Due to an asymmetric design regarding the position of the supply lines relative to the JJs, the current I_Φ required to bias and modulate the magnetic flux can be applied directly to the SQUID loop, without the need to use additional modulation coils.

The junctions incorporated in the SQUIDs have a length of 10 to 30 nm (cf. Fig. 4 (b)), which is in the order of the superconducting coherence length ξ of 15 nm in Nb thin films. Fig. 4 (a) shows the SQUID layout. It features a relatively broad loop to decrease the SQUID inductance partially compensating high kinetic inductance of the ultrathin superconducting Nb film. The rectangular shape of the SQUID loop additionally enhances the resolution of the EBL step, as the electron beam can write parallel to all edges.

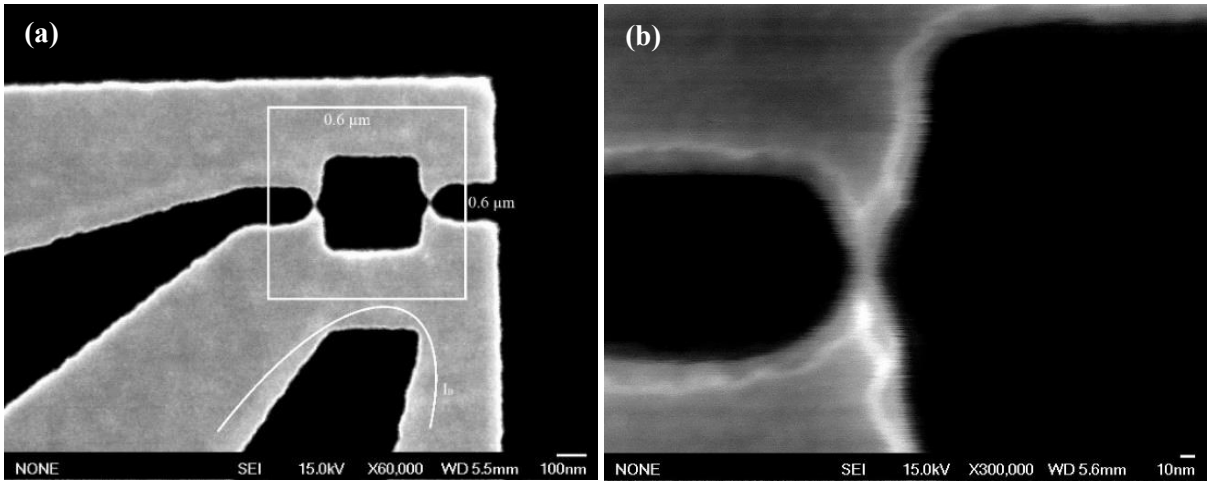

Figure 4. SEM images of a rectangular nanoSQUID with incorporated GDB junctions that have a width of approximately 10 nm.

Grooved Dayem bridges combine the easy fabrication, planarity and flexibility of Dayem bridges with the performance of grain boundary weak links. They have first been fabricated by [7] using the high T_C superconductor YBCO ($YBa_2Cu_3O_{7-\delta}$). Those weak links were later implemented in SQUIDs for SQUID magnetometry. An amorphous hard carbon mask is applied on top of a superconducting layer and structured using EBL. The mask resembles the one of a Dayem bridge but contains a full width gap in the junction. Low energy ion milling through the mask then physically etches the superconductor. The etch rate is reduced in the gap area due to partial redeposition. This way the superconductor is thinned out in the junction area, while besides the junction it is fully etched to the substrate. According to ref. [7], such grooved Dayem nanobridges express large voltage modulation, low white flux noise, low magnetic field noise, a small critical current density and a large resistivity compared to conventional Dayem nanobridges. The latter leads to a reduction of the input noise of the readout electronics.

As can be seen in the TEM image in Fig. 5, we achieve a similar effect as in ref. [7] with their high T_c GDBs when etching two lines of Nb, that are only separated by a small gap of a few nanometres in the mask formed of resist.

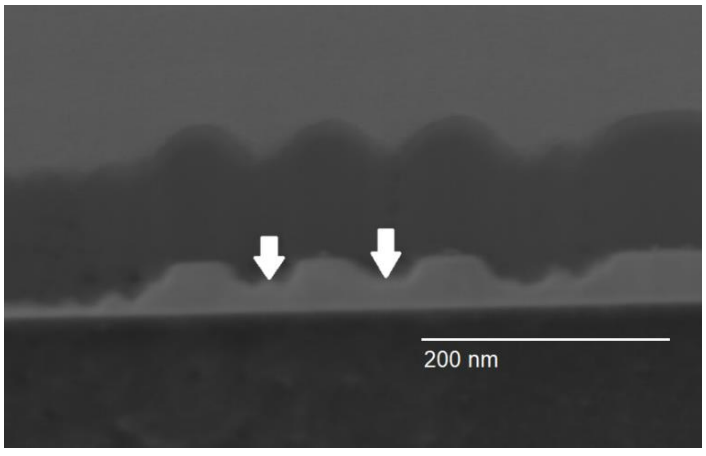

Figure 5. A low resolution TEM image of lines in Nb structured using negPMMA resist and etched in SF_6 for 60s. Areas between the lines where Nb has a reduced etching rate are indicated.

In between the lines, Nb is redeposited, so that in these places a thin Nb layer remains on the substrate. This result is very promising, considering the possibility to produce Dayem bridges that are thinned out in the middle, thus reducing their dimensions even more.

Different slit widths were therefore tested on several JJs. The layout of the chip was similar to the layout described above to test junctions, only that now all seven junctions had a length of 30 nm in the EBL mask with slits ranging from 0 nm to 6 nm. In this case, 0 nm means that there is no slit in the layout, but the electron beam in EBL approaches the middle of the GDB from different sides.

As can be seen in Fig. 6, the 0 nm slit resulted in actual GDBs with a slit in the negPMMA resist but redeposited Nb in the junction. For slits bigger than 2 nm there was no Nb in the junction anymore. The shown samples were prepared using negPMMA resist on an 15 nm Nb film and an etching time of 90 s. In the following, all SQUIDs were fabricated using 0 nm slits.

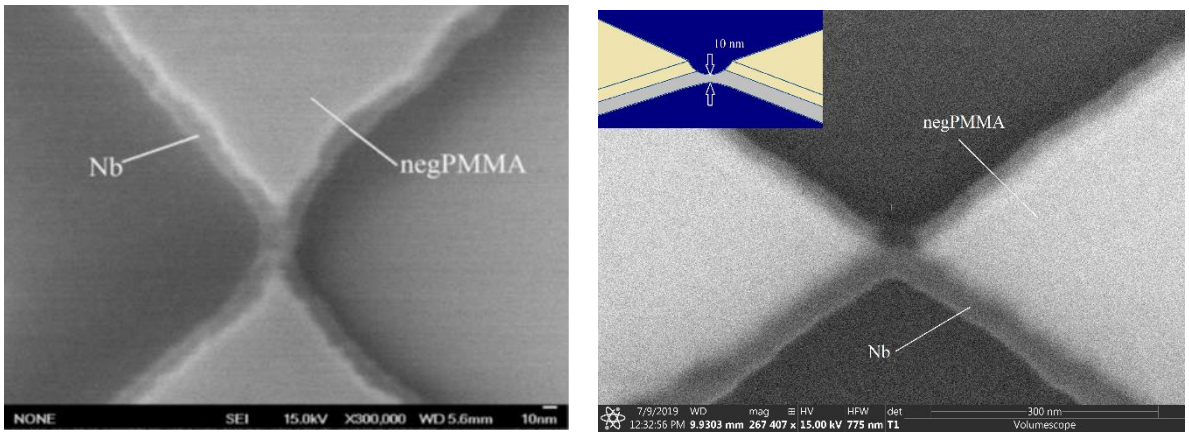

Figure 6. SEM images of a GDB with a slit width in the EBL layout of 0 nm.

3.3. I(V)-characteristics

In a Josephson junction, the *I(V)*-curve can either be hysteretic or non-hysteretic. For a current lower than the critical current I_C there is no voltage across a Josephson junction in the non-hysteretic case. However, when exceeding the critical current, one gets into the region of the AC Josephson effect with a voltage across the junction of $V > 0$ and a phase difference of $\varphi = \omega t$ oscillating with a voltage-dependant circular frequency of $\omega = 2\pi V/\Phi_0$ [16].

For the application in a sensor device, a non-hysteretic DC Josephson effect is desirable. There are three main reasons for the occurrence of such a hysteresis. One of them is described by the *RSJ-model*, or *Resistively Shunted Junction model*. It starts with an equivalent circuit for the junction. It consists of the junction and a parallel capacity and resistance and can be described by the differential equation

$$I(t) = I_C \sin(\varphi) + C\frac{dV}{dt} + \frac{V}{R_n}$$

that can be rewritten as

$$I(\tau) = \beta_C \frac{d^2\varphi}{d\tau^2} + \frac{d\varphi}{d\tau} + \sin(\varphi)$$

using the normalized time $\tau = \frac{\hbar}{2eI_CR_n}$ and the *Stewart McCumber parameter* $\beta_C = \frac{2e}{\hbar} I_C {R_n}^2 C$. For $\beta_C < 1$ one gets an over-damped junction with no hysteresis, while for $\beta_C > 1$ it is underdamped and hysteretic [17]. Thus, the hysteresis can be eliminated by shunting the JJ with an ohmic resistor [16].

Another origin of the hysteresis lays in the geometry of the structure itself, which influences the *Current Phase Relationship* (CPR) $I_s(\varphi)$ of the JJ. In general, the supercurrent I_s through a JJ is periodic in the phase difference φ between the two superconducting electrodes. For junction lengths in the order of the Ginzburg-Landau coherence length ξ_0 the CPR is sinusoidal, while it turns into a tooth-like shape

for larger bridge lengths. After a certain critical length of $L_C \approx 3.5\,\xi(T)$ the CPR becomes multivalued, which suppresses superconductivity above I_C due to phase slippage centres. This is where the Josephson effect is replaced by a one-dimensional depairing effect [9, 14]. This depairing evolves to the so called Abrikosov vortex motion for widths of the JJs $W > W_C$, a coherent motion of vortices in the superconductor, as the phase difference φ relaxes across the junction and a long-range order is preserved [16]. As the coherence length in thin Nb films is $\xi \cong 15$ nm, fabricated JJs need to be of this size in all three dimensions, which requires advanced nanostructuring techniques.

A third possibility is a thermal hysteresis. If the junction is biased with a current, the nanobridge can heat up above the critical temperature T_C, thus destroying superconductivity and leading to a hysteresis in the *I(V)*-characteristics. To prevent this, we have coated the SQUIDs with a layer of Si after RIE. At 4.2 K this acts as a thermal shunt of the weak link, while at 300 K it's electrically shunting off the bridge [15].

The I*(V)*-curve of a 10nm nanobridge JJ was measured at 4.2 K using home-made PC-controlled low noise electronics (Fig. 7). The *I(V)*-curve displays hardly any hysteresis, a normal state resistance of $R_N \cong 40\ \Omega$ and a critical current of $I_C \approx 6\ \mu A$ at 4.2 K. The corresponding McCumber parameter β_C of the individual junction is approximately 1, if we attribute the hysteresis exclusively to the capacitance C, normal state resistance R_N and critical current I_c in our junctions. In that case, this would correspond to an effective capacitance of the junction of approximately 34 fF.

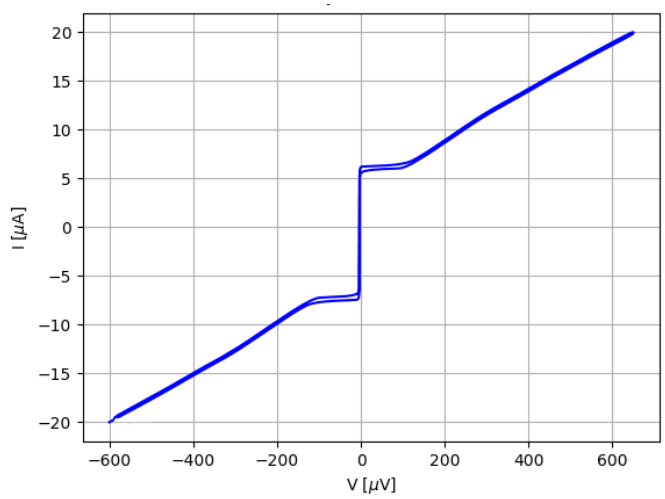

Figure 7. *I(V)*-characteristics of a nanobridge measured at 4.2 K showing an almost non-hysteretic behaviour.

3.4. Flux modulation and SQUID response

By applying a bias current I_B to the SQUID as described in subsection 3.2, a magnetic flux through the SQUID loop is induced, that modulates the voltage across the SQUID. The induced flux directly depends on the geometrical inductance of our sample, which is given by $L \approx 2 \cdot l \cdot \left(ln\frac{2l}{b} + 0.75\right)\frac{\mathrm{nH}}{\mathrm{cm}}$, where the units for length and inductance are in cm and nH, respectively, l is the length and b the width of the part of the SQUID loop where the bias current flows [18]. If we insert $l = 500$ nm and $b = 300$ nm, we get a geometrical inductance of $L \approx 0.14$ pH, which leads to an experimentally observed induced flux of about $0.68\ \Phi_0$ for a flux bias current of $I_\Phi = 10$ mA.

Fig. 4 (a) shows a nanoSQUID with incorporated 10 nm GDBs that was used for the measurement of flux modulations. The SQUID was fabricated using an HSQ mask on a ca. 38 nm thick film of Nb,

that was etched using SF_6 for 45 s. Using the integrated flux bias, we have measured one full period of SQUID modulations for $I_B > 0$ and one full period of SQUID modulation for $I_B < 0$, respectively.

Using a Quantum Design physical property measurement system (PPMS), we have plotted seven full periods of the SQUID modulation of another SQUID fabricated using negPMMA (cf. Fig. 8). One full period of the SQUID modulation *V(Φ)* is 6 mT, which corresponds to an effective area of the nanoSQUID of 0.3 μm^2. This effective area is shown as a white square with the edge length of 0.6 μm in Fig. 4(a). The measurements were conducted at different bias currents close to the critical current. The tested SQUID shows a wide range of currents between 11 μA and 13.5 μA, in which the oscillations are cosinosodial. For higher currents, the curve displays dips resulting from parabolic SQUID oscillations with negative sign, while for lower currents the parabolas display a positive sign. This was the expected behaviour as can be seen in Fig.1 in ref. [19]. As we have single-valued CPRs and a critical voltage comparable with its value in the tunnel junction, we observe an *ideal Josephson effect* as defined in Ref. [8] as "the case where the [current-phase] relationship is single-valued and [the critical voltage] is comparable with its value in the tunnel junction".

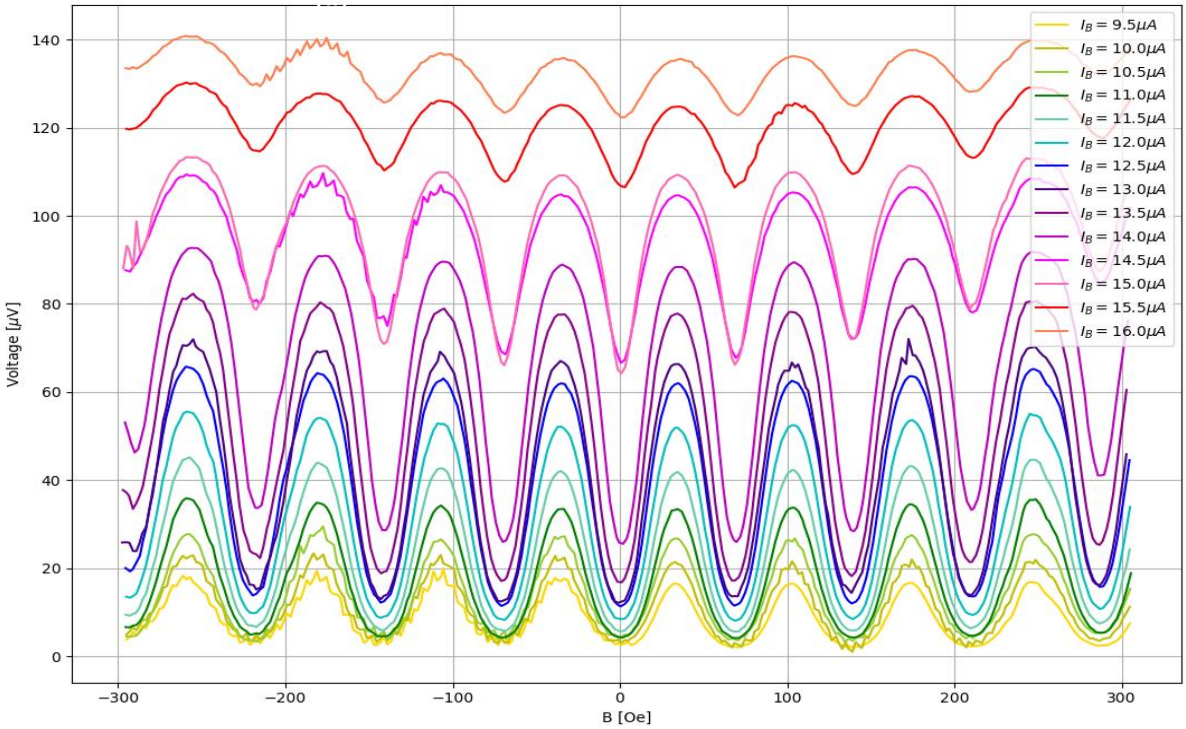

Figure 8. SQUID modulation *V(Φ)* measured using a Quantum Design PPMS for different SQUID bias currents close to $I_B \cong 2I_c$. The uppermost curve was measured at the highest and the bottom curve at the lowest critical current. All curves in between are sorted accordingly

The energy resolution of DC SQUIDs is limited by Jonson noise in the resistive shunts. At sufficiently low temperatures $T << eI_cR_n/k_B$ the dominant noise source is shot noise in the junctions [20] and can be written as

$$E_R^{(dc\ SQUID)} = \frac{S_\Phi(0)}{2L} \geq \hbar$$

with the pickup loop inductance L and the equivalent flux-noise power spectral density $S_\Phi(\nu)$ depending on the frequency ν and the magnetic flux through the loop Φ. Small SQUIDs have reached down to

$E_R^{(dc\ SQUID)} \approx 2\hbar$ [20-22]. Different magnetometers approach an energy resolution of $E_R = \hbar$, that can be a universal quantum limit for the whole span of low noise magnetic field sensing technologies [24].

The effective inductance of a nanoSQUID that contributes to the flux noise and energy resolution of the nanoSQUIDs is governed by the kinetic inductance of the loop [5] $L_k = 2\pi\mu_0\lambda_L^2 r/a$ that is approximately 40 pH for the average size of the nanoSQUID shown in Fig. 4(a) with $r \cong 400$ nm, a cross-section area of a = 400 nm x 60 nm and λ_L = 560 nm [5]. At 4.2 K the energy sensitivity of the nanoSQUID is limited by the Johnson noise [20]:

$$\frac{S_\Phi}{2L} = \frac{S_V}{\left(\partial V/\partial\Phi\right)^2 2L_k} = \frac{16 k_B T R_N}{\left(\partial V/\partial\Phi\right)^2 2L_k} \cong 452\ \hbar\,,$$

where the value $\partial V/\partial\Phi \cong 188\ \mu V/\Phi_0$ was obtained from Fig. 8 and $R_N = 35\ \Omega$ from Fig. 1 (b). Thus an estimated flux sensitivity $S_\Phi^{1/2} \cong 1\ \mu\Phi_0/\sqrt{\text{Hz}}$, a magnetic field resolution $B_N = \left(\partial B/\partial \Phi\right) S_\Phi^{1/2} \cong 6\ \text{nT}/\sqrt{\text{Hz}}$ and a spin sensitivity $S_n^{1/2} = S_\Phi^{1/2}\frac{r}{r_e} \cong 135\ \mu_B/\sqrt{\text{Hz}}$ is obtained, where $r_e = 2.82 \times 10^{-15}$ m is the classical electron radius [25].

4. Summary and outlook

We have shown that it is possible to fabricate nanoSQUIDs incorporating Dayem nanobridges with a length of only 10 to 30 nm using HSQ electron beam resist and reactive ion etching in pure SF_6. Results with the same resolution were achieved using PMMA as a high resolution negative resist. This leads to an additional photolithography step being necessary, but has advantages in resist availability, resist shelf life and a lower health risks. The fabricated nanoSQUIDs were tested and showed nonhysteretic *I(V)*-characteristics at 4.2 K. The nanoSQUIDs show a voltage modulation by a directly injected magnetic flux as well as by an externally applied flux of a magnetic field, which makes them suitable as high resolution magnetic spin sensors. The obtained spin sensitivity of $S_n^{1/2} = 135\,\mu_B/\sqrt{Hz}$ is very promising for the use of the nanoSQUIDs as magnetic sensors for nanoscale objects. Further improvement of the spin sensitivity is possible by the further miniaturization of the SQUID loop.

The nanoSQUIDs fabricated using the nanofabrication techniques described above will be implemented in a high resolution SSM for future measurements of magnetic samples with projected single spin resolution. The SSM currently under construction uses attocube's positioning and scanning stages. The specified measurement range is up to 5 mm with sub-nm resolution at 4.2 K. The sample will be fixed on attocube's sample holder that has an integrated heater to perform thermal cyclings and temperature stabilization during the measurements. The SQUID chip will comprise a Si substrate with a lithographically patterned step at the corner where the SQUID is placed. During the scanning process, the lithographically fabricated step will provide a minimal distance of the nanoSQUID from the corner of the substrate and, therefore, from the mechanical contact to the scanned surface.

The developed nanoSQUID sensors will also be used to create a number of devices for conducting physical measurements, in particular, in actively developing fields of studying the magnetic properties of new and exotic materials, metamaterials, spontaneous currents in pi-loops [26] and nanorings of normal metals [27], as well as spintronics nanoobjects (magnetic nanobridges, nanowires, spin-valve structures, skyrmions, surface currents in topological isolate edges, edge currents in structures with a quantum Hall effect, etc.) at nanometer sizes with a projected spin sensitivity in the order of 1 $\mu_B/\sqrt{\text{Hz}}$. The developed superconducting nanobridges with a size in the order of 10 nm will also serve as the main active elements of the new superconducting nanobridge electronics [28, 29] designed for next generation quantum devices.

Acknowledgements

This work was supported by the PGI-5 FZJ CEI E-Project (E.23102.76). The authors gratefully acknowledge fruitful discussions with V. S. Stolyarov, the possibilities to perform important parts of the

work at ER-C-1, HNF, PGI-4/JCNS-2, PGI-5 and PGI-7 of the Forschungszentrum Jülich GmbH and the technical assistance of H. Stumpf, S. Trellenkamp, F. Lentz, S. Nandi, and R. Borowski.

References

[1] Foley C P, Hilgenkamp H 2009 *Superconductor Science and Technology* **22** 064001
[2] Zimmerman J E and Mercerea J E 1964 *Phys. Rev. Lett*. **13** 125
[3] Vu L N and van Harlingen D J 1993 *IEEE Trans. Appl. Supercond*. **3** 1918
[4] Faley M I et al. 2017 *IEEE Transactions on Appl. Supercond*., **27**, No.4, 1600905
[5] Troemann A 2007 PhD thesis, University of Twente, Netherlands
[6] Finkler A et al. 2010 *Nano Letters* **10** 1046
[7] Anderson P W and Dayem A H 1964 *Physical Review Letters* **13** 195–197
[8] Trabaldo E et al. 2019 *Nano Letters* **19** 1902–1907
[9] Likharev K 1979 *Rewiews of modern Physics* **51** 101
[10] Lemberger T R 2007 *Physical Review B* **76** 094515
[11] Faley M I et al. 2017 *Superconductor Science and Technology* **30** 083001
[12] Macintyre D S et al. 2006 *Microelectronic Engineering* **83** 1128–1131
[13] Charaev I et al. 2017 *Journal of Applied Physics* **122** 083901
[14] Hoole A C F 1997 *Semiconductor Science and Technology* **12** 1166–1170
[15] Holdeman L B and Peters P N 1976 *Applied Physics Letters* **28** 632–634
[16] Walke P 2010 PhD thesis, University of Naples, Italy.
[17] Waser R 2012 "Nanoelectronics and Information Technology" 3rd. Weinheim: Wiley-VCH.
[18] Nührmann D 1998 "Das große Werkbuch Elektronik" Franzis' Band1 p. 732
[19] Mijatovic D et al. 2005 *Applied Physics Letters* **8** 192505
[20] Tesche C D and Clarke J 1977 *Journal of Low Temperature Physics* **29** 301
[21] Awschalom D D et al 1988 *Applied Physics Letters* **53** 2108
[22] Mück M 2001 *Applied Physics Letters* **78** 967
[23] Wakai R T and Van Harlingen D J 1988 *Applied Physics Letters* **52** 1182
[24] Mitchell M W et al. 2019 arXiv:1905.00618
[25] Ketchen M B et al. 1989 *IEEE Trans. Magn*. **25** 1212
[26] Faley M I et al. 2019 *IEEE Transactions on Applied Superconductivity* **29** 1100405
[27] Bluhm H et al., 2009 *Phys. Rev. Lett*. **102** 136802
[28] Shelly et al. 2017 *Superconductor Science and Technology* **30**, 095013
[29] Collins J 2019 European Conference on Applied Superconductivity EuCAS'2019 in Glasgow